PERGAMON

International Journal of Heat and Mass Transfer 45 (2002) 4995–5005

International Journal of HEAT and MASS TRANSFER

www.elsevier.com/locate/ijhmt

Liquid–solid separation phenomena of two-phase turbulent flow in curved pipes

Hui Gao, Liejin Guo *, Ximin Zhang

State Key Laboratory of Multiphase Flow in Power Engineering, Xi'an Jiaotong University, 710049 Xi'an, Shaanxi, PR China

Received 4 January 2002; received in revised form 20 May 2002

Abstract

The present study is to contribute some knowledge of phase separation phenomena of liquid–solid two-phase turbulent flow in curved pipes and provide a basis for the invention and development of a new type of curved pipe separator. Firstly, the solid–liquid two-phase flows in two-dimensional (2D) curved channels were numerically simulated using a two-way coupling Euler–Lagrangian scheme. Phase distribution characteristics of 2D curved channel two-phase flow were examined under conditions of different particle size, liquid flowrate and coil curvature. Based on the numerical results, the dynamic effects and contributions to phase separation of particle-subjected forces, including centrifugal force, drag force, pressure gradient force, gravity force, buoyancy force, virtual mass force and lift force, were exposed by kinematic and dynamic analysis along particle trajectories. Secondly, measurement of particle size and concentration profiles in helically coiled tube two-phase flow was conducted using a nonintrusive Malvern 2600 particle sizer based on laser diffraction. Particle size and concentration distribution characteristics of helically coiled tube two-phase flow and the effect of secondary flow on phase separation were analyzed based on experimental data.

Keywords: Curved pipe; Phase separation; Turbulence; Liquid–solid two-phase flow; Numerical simulation

1. Introduction

Single or multi-phase flows in curved pipes are frequently encountered in industry, for example, gas–solid two-phase flow in the turning of pneumatic conveying pipelines, oil–gas two-phase flow or oil–gas–water three-phase flow in helically coiled tube heat exchangers in petroleum and chemical industries. Phase separation occurs in all kinds of curved pipe because of the differences in the inherent centrifugal force, gravity force and secondary flow effect between heavy and light phases. It influences the pressure loss of fluid flow as well as the heat and mass transfer performance. Particularly in liquid–solid two-phase flows through curved pipes, particles are driven from inner bend to outer bend by centrifugal effect. Phase separation phenomenon was recognized and utilized to invent a new type of separator. The understanding of the mechanisms and experimental research on it was motivated.

Curved pipe separator found its first application in petroleum industry. Sand is often carried from wells in addition to oil–water emulsions and natural gas streams, and thus present a multi-phase separation problem. Desanding is vital because the coexistence of sand and oil would cause serious wearing and clogging problems to the operational facilities and equipment. Although sediment tank [1] and hydrocyclone [2,3] desanding techniques have been developing until now, the problem remains unsolved for obvious drawbacks of both ones, i.e. the former occupies large ground area and hence could not be used in offshore hydrocarbon production, while the latter leads to a high pressure loss and

* Corresponding author. Tel.: +86-29-2663895; fax: +86-29-2668769.

E-mail address: lj-guo@mail.xjtu.edu.cn (L. Guo).

0017-9310/02/$ - see front matter
PII: S0017-9310(02)00207-7

Nomenclature

C_D, C_{am}	modeling coefficients
d_p	particle diameter (m)
f	correction factor of Saffman lift force
$\vec{e}$	unit vector
g	gravity ($m\,s^{-2}$)
H	height of cross-section (m)
k	turbulent kinetic energy ($m^2\,s^{-2}$)
L_1, L_2	length of straight parts (m)
n	Rosin–Rammler model parameter
p	pressure (Pa)
R	curved radius (m)
R_{c1}, R_{c2}	coil radius (m)
Re	liquid flow Reynolds number
Re_p	particle Reynolds number based on relative velocity between phases
S	deformation rate tensor (s^{-1})
T_L	fluid Lagrangian integral time (s)
u	fluid velocity ($m\,s^{-1}$)
u_p	particle velocity ($m\,s^{-1}$)
V_m	fluid mean velocity ($m\,s^{-1}$)
X	Rosin–Rammler model parameter (m)
x	descartes coordinate (m)
y^+	dimensionless distance from the wall to the nearest grid cell

Greek symbols

β	volume concentration of particle phase
β_0	averaged volume concentration of particle phase
ε	dissipation rate of turbulent kinetic energy ($m^2\,s^{-3}$)
η_{90}	a classification efficiency
μ	fluid dynamic viscosity ($kg\,m^{-1}\,s^{-1}$)
θ	curve angle (°)
ν	fluid kinetic viscosity ($m^2\,s^{-1}$)
ξ	dimensionless radius
ξ_0	dimensionless radius of particle releasing position
ρ	fluid density ($kg\,m^{-3}$)
ρ_p	particle density ($kg\,m^{-3}$)
σ	normally distributed random number
ψ	particle cumulative mass distribution

Subscripts

i, j, k	descartes coordinate directions
i, o	inner bend, outer bend

Superscripts

$'$	fluctuation value in time averaging
-	averaged value

demands the utilization and frequent replacing of multi-phase pumps and thus costs too much. Accordingly, curved pipe separator was invented to overcome these problems and proved to be effective in pilot scale in situ experiment [4]. Comparing with the conventional separation techniques, curved pipe separator has many advantages, such as simplicity and compactness in structure, high efficiency and low pressure loss over them. Up to now, it also promises well in more extensive applications from hydroelectric engineering to industrial waste water processing. The development of this new separation technique makes it urgent to know about phase distribution in such flows and understand of the key mechanisms responsible for phase separation.

Comparing with numerous investigations of single-phase flow [5], gas–liquid two-phase flow and oil–gas–water three-phase flow [6,7] through curved pipes, only limited information regarding the liquid–solid two-phase flow is available in literature. Kaimal and Devanathan [8] solved a developing two-phase laminar flow in curved tube using two-fluid model and asymptotic method. Xu et al. [9] numerically studied liquid–solid two-phase turbulent flow in curved pipe employing two-fluid model and finite element method. Up to now, few experimental data is available and the numerical studies scarcely considered the mechanism of particle dynamics.

The purpose of the present study is to depict the particle size and concentration profiles in curved pipe two-phase turbulent flow, and to both qualitatively and quantitatively evaluate the contribution of centrifugal effect, various hydraulic forces, secondary flow and turbulent dispersion to phase separation. Two-dimensional (2D) curved channel is a simplified model of actual duct with small cross-section aspect ratio (height over width). It has great engineering importance because secondary flow is restrained in this case and thus its negative effect is eliminated. Further more, by excluding the complicated secondary flow effects, it is more convenient to quantify the contribution of centrifugal effect, turbulent dispersion and other hydraulic forces on separation. Therefore, two-phase flows through 2D curved channels were firstly numerically simulated. Particle concentration profiles were depicted for various flow situations and particle dynamic analysis was performed along particle trajectories. Secondly, particle size and concentration profiles in two-phase flows through a helically coiled tube, which is a smaller model of the pilot scale separator, were measured to examine the effect of secondary flow. The presented results and analysis will be helpful to improve both the theory of curved pipe multi-phase flow modeling and the design of the innovative separator.

2. Numerical and experimental models

2.1. Physical model for 2D curved channel two-phase flow numerical simulation

2.1.1. Geometric configuration and flow parameters

As shown in Fig. 1, the 2D curved channel consists of a 270° part with a curvature radius of R_{c1} and a 90° part with a curvature radius of R_{c2}, and is preceded and followed by straight parts with length of L_1 and L_2, respectively. H is the height of the cross-section. Three curved channels, with their coil axis all horizontally positioned, were considered in this paper. Detailed geometrical parameters are shown in Table 1.

Liquid flow Reynolds number Re covers a range of $(8–30)\times 10^4$. Water was selected as conveying fluid, with density $\rho = 0.998\times 10^3$ kg m^{-3} and viscosity $\mu = 1.003\times 10^{-3}$ Pa s. Solid phase was selected as sand with density of $\rho_p = 2.8\times 10^3$ kg m^{-3} and considered as sphere with diameter d_p ranging from 50 to 400 μm. The averaged particle volume concentration β_0 is 0.1%.

2.1.2. Euler–Lagrangian two-phase flow model

A two-way coupling Euler–Lagrangian two-phase flow model was used in the numerical simulation. Firstly, the liquid phase flow was solved utilizing the Reynolds stress model along with a near wall low-Re turbulence model. Secondly, particle trajectories were calculated by integrating the particle motion equation and the trajectory equation, and the particle source term in liquid phase momentum equation was computed simultaneously. Then a new iterative loop was started until a converged solution was achieved, i.e. both continuous phase flow field and particle trajectories would be nearly unchanged with each additional calculation.

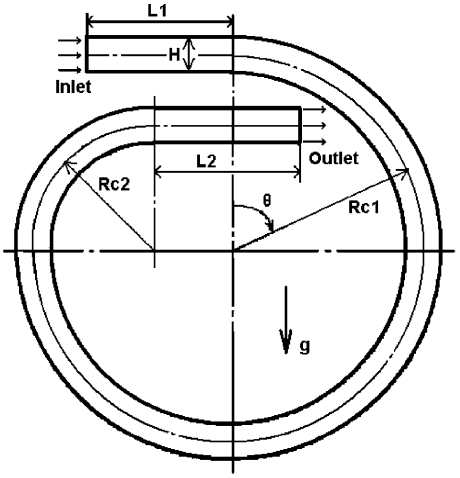

Fig. 1. Sketch of a 2D curved channel.

Table 1
Geometrical parameters of curved channels (unit: m)

No.	H	L_1	R_{c1}	R_{c2}	L_2
1	0.038	0.127	0.175	0.111	0.127
2	0.038	0.127	0.140	0.089	0.089
3	0.038	0.127	0.105	0.067	0.071

The force law, or particle motion equation, including inertia force, drag force, pressure gradient force, virtual mass force, gravity and buoyancy force, and lift force, can be written as

$$\frac{du_{p,i}}{dt} = \frac{18\mu}{\rho_p d_p^2}\frac{C_D Re_p}{24}(u_i - u_{p,i}) - \frac{1}{\rho_p}\frac{\partial p}{\partial x_i} + C_{am}\frac{\rho}{\rho_p}\frac{d}{dt}(u_i - u_{p,i}) + \left(1 - \frac{\rho}{\rho_p}\right)g_i + \frac{2fKv^{1/2}\rho S_{ij}}{\rho_p d_p (S_{lk}S_{kl})^{1/4}}(u_j - u_{p,j}), \quad i,j = 1,2 \tag{1}$$

where, drag coefficient C_D is computed by Morsi and Alexander's correlation [10], the virtual mass coefficient $C_{am} = 0.5$, and f is a correction factor of Saffman force proposed by Mei [11]. The trajectory equation is as follows:

$$\frac{dx_i}{dt} = u_{p,i}, \quad i = 1,2 \tag{2}$$

Turbulent dispersion is a complicated phenomenon that affects particle motion notably. Here it was modeled by a Monte Carlo method [12], in which instantaneous fluid velocity is used in the integration of the particle trajectory equation. The fluctuating velocity components are piecewise constant functions of time, i.e. they are sampled by assuming that they obey a Gaussian probability distribution and keep unchanged over the lifetime of the turbulent eddy

$$u_i' = \sigma\sqrt{\overline{u_i'^2}} = \sigma\sqrt{2k/3} \tag{3}$$

where σ is a normally distributed random number. The eddy lifetime equals to the fluid Lagrangian integral time and is computed as follows:

$$T_L = 0.3\frac{k}{\varepsilon} \tag{4}$$

2.1.3. Numerical scheme

The computation of continuous flow is based on the control volume method. Second-order upwind scheme was used in the discretization of differential equations. SIMPLEC algorithm was used for pressure–velocity coupling. Velocity boundary condition was used at the inlet. Pressure boundary condition was used at the outlet. No-slip boundary condition and reflecting condition were used at walls for liquid phase and solid

phase, respectively. Nonuniform grids were arranged in the lateral direction, with 30 intervals increasing in size from the wall to the center at the rate of 1.05. While in the streamwise direction, uniform grids were arranged with 40 intervals in each quarter of the curved part and 20 intervals in each straight part. By performing solution-adaptive grid refinement, the dimensionless distance from the wall to the nearest grid, y^+, is below 5, which satisfies the mesh requirement of the low-*Re* turbulence model. Particle tracking is an initial condition problem of ordinary differential equation. It was solved by using fourth-order Runge-Kutta method.

2.2. Experimental model for phase distribution measurements

2.2.1. Experimental facilities and test section structure

The experimental set-up consists of water–sand two-phase flow test loop, helically coiled tube test section and Malvern measurement system. The test loop is schematically illustrated in Fig. 2. A common water pump was used instead of the costly two-phase flow pump because online mixing and separating technique was utilized. Water flowrate was measured using two orifice meters with different flow ranges, which were calibrated prior to the experiment. Since it is essential to maintain accurate and stable sand flowrate in particle size and concentration measurement process, we designed and constructed a sand flowmeter. Sands were fed into the flowmeter from sand tank and then dropped through an rotating impeller into the water–sand mixer due to gravity. Sand flowrate is directly proportional to rotating velocity of the impeller. The impeller was driven by a speed-changeable motor, the speed of which is proportional to the adjusting voltage supplied by a transformer. Before experiment, sand flowrates were measured using a weighting method under the condition of various transformer output voltages. It shows that sand flowrate and transformer output voltage is linear fitted with an error <1%. The correlation was then used in later experiment. Online mixing was achieved by a water–sand mixer, in which a stable air–water interface was formed and sands dropped through air space into

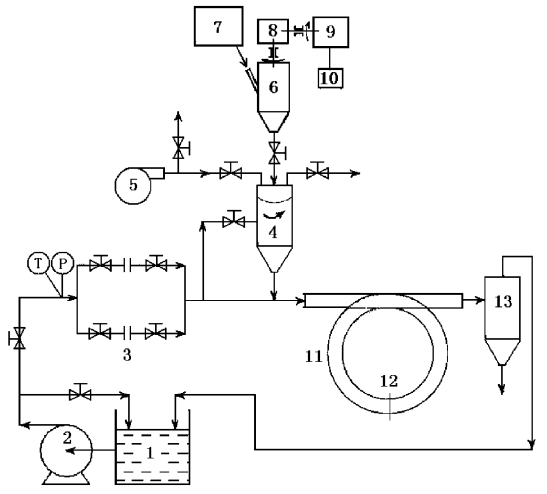

Fig. 2. Water–sand two-phase flow test loop. (1) water tank, (2) water pump, (3) orifices, (4) water–sand mixer, (5) air compressor, (6) sand meter, (7) sand tank, (8) transmission, (9) speed-changeable motor, (10) transformer, (11) test section, (12) measurement plane, (13) filter, P: pressure meter, T: thermocouple.

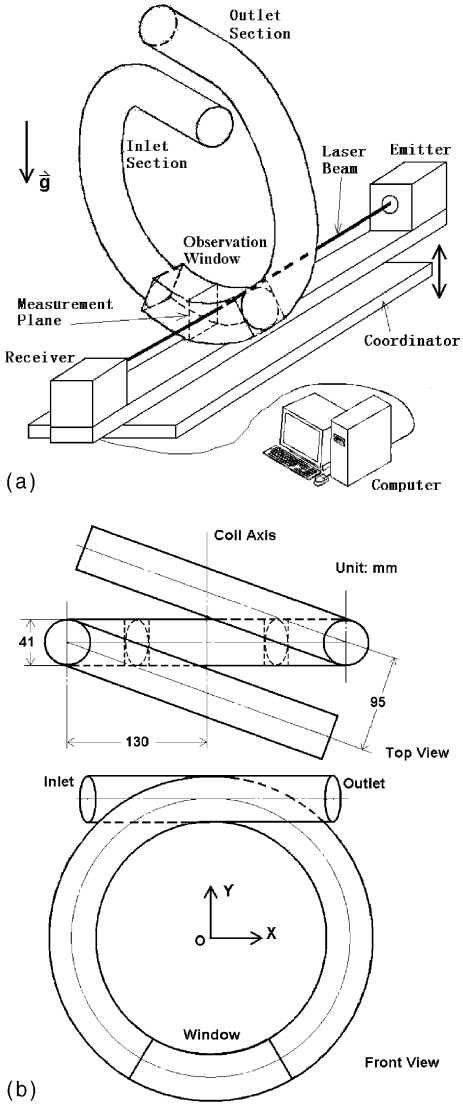

Fig. 3. (a) Helically coiled tube test section and Malvern particle sizer; (b) top and front view of the helically coiled tube.

water. Water was tangentially injected into the mixer to facilitate mixing.

As shown in Fig. 3, the test section consists of three parts: inlet section, observation window and outlet section. Both inlet section and outlet section were manufactured by joining a straight circular tube and a 150° curved circular tube with curvature diameter of 260 mm. The inner diameter of tube is 41 mm. The observation window has a 41×41 mm square cross-section and forms a 60° curved duct with the same curvature as other curved sections. A piece of optical glass was mounted to each side of the observation window to create an optical access. The observation window was connected with inlet section and outlet section by flanges to assemble a helically coiled tube with pitch of 95 mm. The coil axis of the test section was horizontally positioned. The observation window located at the bottom of the coil.

Malvern 2600 particle sizer which is based on laser diffraction technique was used for sand size and concentration measurement. It was placed on a one-dimensional coordinator and aligned perpendicularly to the observation window. By moving the coordinator in the vertical direction, sand size and concentration profiles on the 180° cross-section (i.e. the measurement plane) were obtained. Each data point corresponds to the average information of the measurement volume (a cylinder with diameter of 7 mm and height of 41 mm). A lens with focus of 300 mm was used and thus the particle size range of 5.8–564 μm was covered to satisfy experimental requirement.

2.2.2. Parameter ranges and experimental procedure

The present experiment covers following parameter ranges: the average velocity of water $V_m = 1.0$–$1.7\ \mathrm{m\,s^{-1}}$, sand average volume concentration $\beta_0 = 0.1$–0.3%. Sands were taken from Shengli oil field in east China and have a density of $2.8 \times 10^3\ \mathrm{kg\,m^{-3}}$. The procedure for experiment is as follows:

1. start the water pump and establish water flowrate;
2. turn on the air compressor, then adjust the valves at air inlet and outlet of the mixer to form a stable air–water interface in it;
3. open the valve between the mixer and sand flowmeter and switch on the Malvern particle sizer;
4. move the coordinator to locate the laser to the lower limit of the measurement plane;
5. adjust the alignment of emitter and receiver and measure light background, then turn on the motor and establish sand flowrate; when steady flow is reached, collect 2000 data samples and process and record the information by computer; repeat measurement three times and then turn off the motor;
6. move the coordinator upwardly by 2–4 mm and repeat step 5 until the upper limit of the measurement plane is reached;
7. repeat the above procedure for new operating parameters.

2.2.3. Data reduction and uncertainties analysis

Sands used in present experiment should be considered as a polydisperse system. Rosin–Rammler model was used to represent particle size distribution

$$\psi(d_p) = \exp[-(d_p/X)^n)] \tag{5}$$

where, $\psi(d_p)$ is cumulative mass distribution, X and n are model parameters correspond to particle characteristic size and particle size range, respectively. Measurement results for each position were averaged in an integral way. Firstly, a particle size domain from 5 to 500 mm was uniformly discretized into 49 sections. Then, as shown in Eq. (6), the measured mass frequency in each section was concentration-weighted averaged. Fitting was finally performed, i.e. X and n were varied and the mass frequency in each section were computed by the Rosin–Rammler model, and then a set of model parameters were selected when the sum of square roots of difference between the averaged and calculated value achieved a minimum.

$$\mathrm{d}\psi(d_p) = \frac{1}{3\overline{\beta}} \sum_{i=1}^{3} \beta_i \mathrm{d}\psi(d_p)_i, \quad \overline{\beta} = \frac{1}{3} \sum_{i=1}^{3} \beta_i \tag{6}$$

Fig. 4 presents an example of data averaging at a single measurement position in a flow case. Among all the measurement positions of all the flow cases, the maximum standard deviation of β, X and n achieve about 1.5%, 6% and 20%, respectively. According to the calibration of water loop orifices and sand flowmeter, the errors of water and sand flowrate measurement are

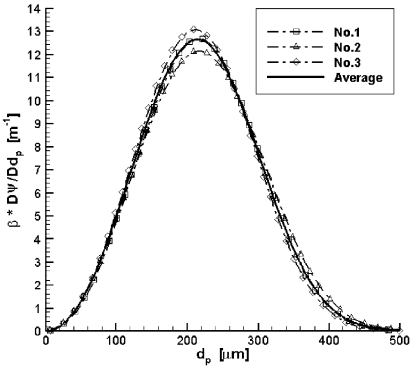

	No.1	No.2	No.3	Average	Standard Deviation (%)
β (%)	0.260	0.262	0.264	0.262	0.7
X (μm)	246	250	241	246	1.9
n	3.07	2.95	3.05	3.02	2.3

Fig. 4. Integral average of measurement results.

±0.4% and ±1%, respectively. Measurement uncertainty of sand concentration including both statistical and systematical errors is hence estimated to be within ±2.9%.

3. Solid particle phase distribution and separation phenomena

3.1. Phase separation phenomena in 2D curved channel two-phase flows

A systematical study of liquid–solid two-phase flow in 2D curved channels were numerically performed. Particle phase distribution and dynamic characteristics were presented for various flow conditions.

3.1.1. Particle concentration profiles

The knowledge about particle concentration and size distribution is the base of particle discharging assembly design and separation efficiency prediction. On the basis of two-way coupling simulation of mono-dispersed two-phase flows, particle concentration profiles on the cross-section of $\theta = 180°$ were computed and illustrated for the cases of various particle sizes, liquid flowrates and channel configurations.

Turbulent dispersion effect was included in the simulation. Particles were released from 20 positions uniformly distributed on the curved part entry cross-section. 25 particles were released from each position. Preliminary simulations with 5, 10, 15, 20, 25 and 30 particles for each releasing position were performed, it shows that the concentration profile of the last two cases differ slightly. Therefore, the 500 particles was considered to represent the dispersed phase statistically.

A new quantity of classification efficiency, η_{90}, which is defined as the separation efficiency of mono-disperse flow with the assumption that particles in the area of $\xi > 0.9$ are collected completely, is introduced here for the purpose of fairly evaluating the separation effect of each flow case.

As seen in Fig. 5(a), the concentration curves can be classified into "plateau-peak" and "slope-peak" two types. The curves for small particles belong to the former. Under this condition, the particles released near the inner wall could only shift to the middle part of the cross-section before $\theta = 180°$. The middle part of the cross-section loses particles to outer bend and gains particles from inner bend with local particle concentration nearly unchanged, therefore the "plateau" is formed there. At the same time, outer bend boundary layer gains particles from the middle part, which making local particle concentration increase sharply and the "peak" appear. It should be noted that the plateau decline near outer bend and this is more prominent for smaller particles. Each curve possesses a "slope" near

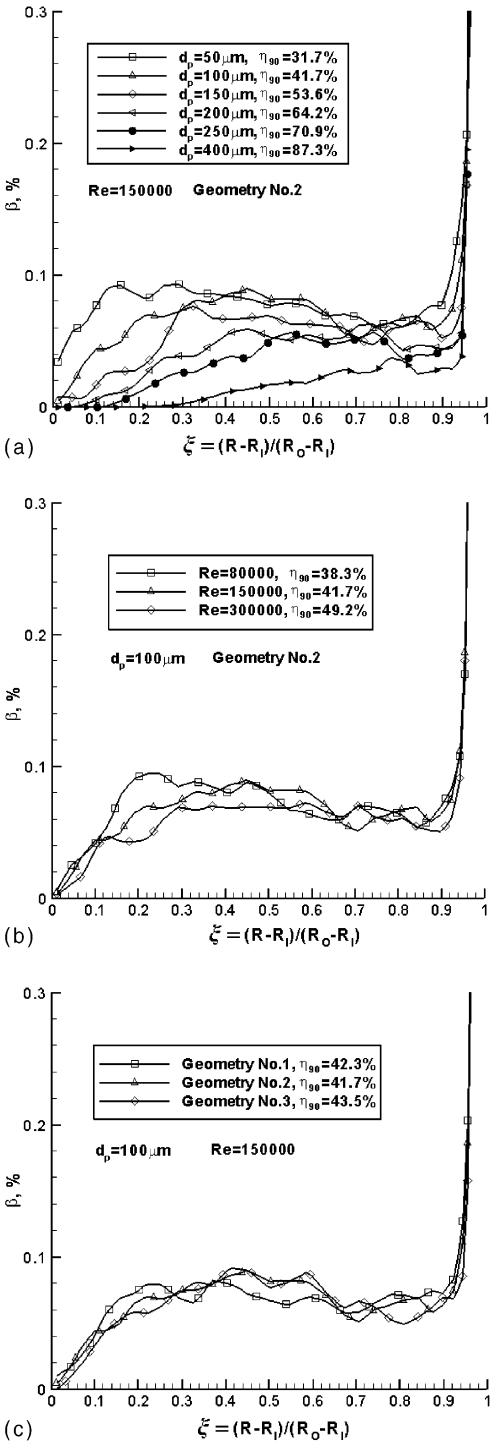

Fig. 5. (a) The effect of d_p on particle concentration profile in 2D curved channel two-phase flow; (b) the effect of *Re* on particle concentration profile in 2D curved channel two-phase flow; (c) the effect of coil curvature on particle concentration profile in 2D curved channel two-phase flow.

inner bend. With the increase of particle size, the slope is continually elongated and finally the curve becomes the slope-peak type, because more and more particles could reach outer bend. Consequently, it give us some ideas about how to design the particle discharging assembly: (i) the discharging "mouth" should just cover the concentration peak; and (ii) the assembly should be located where slope-peak type profile is already formed.

High separation efficiency is achieved for large particles as shown in Fig. 5(a). Small particles are difficult to separate. Fig. 5(b) shows concentration profiles of 100 μm sands under the condition of different liquid flowrate. When the liquid flowrate doubles (*Re* increases from 1.5×10^5 to 3×10^5), the separation efficiency is increased by only 7.5%. Fig. 5(c) presents sand concentration profiles of 100 μm sands under the condition of various channel curvatures. It shows that using tight curvature has little effect on increasing separation efficiency. Channel 2# achieves the lowest value. Thus unfortunately, separation efficiency for small particles could not be raised by just increasing channel curvature, or could only be increased limitedly by increasing liquid flowrates, because centrifugal effect is strengthened at the cost of reducing separation time under each condition. The number of coils and hence the pressure loss over the separator should be increased for this situation.

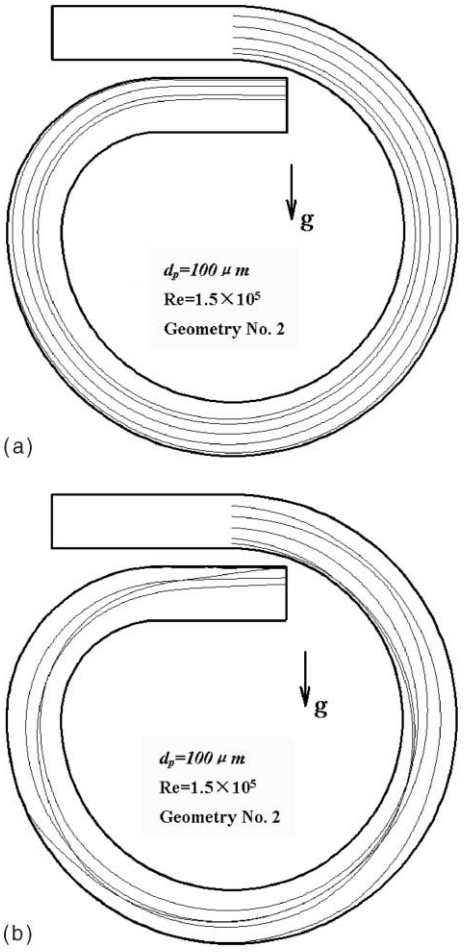

Fig. 6. (a) Particle trajectories in 2D curved channel two-phase flow when excluding turbulent dispersion; (b) particle trajectories in 2D curved channel two-phase flow when including turbulent dispersion.

3.1.2. Particle trajectories

Fig. 6 shows the computed particle trajectories under the condition of excluding or including turbulent dispersion effect. As shown in Fig. 6(a), particles are driven to outer bend by the centrifugal force. When taking into account the effect of turbulent dispersion, as shown in Fig. 6(b), the trajectories become somewhat irregular due to strong randomicity, indicating that turbulent dispersion has a negative effect on phase separation.

3.2. Phase separation phenomena in helically coiled tube two-phase flows

Phase distribution in the flow through the helically coiled tube test section was experimentally investigated. The experimental results were compared to the numerical data of 2D curved channel flow for the purpose of revealing the effect of secondary flow on phase separation.

3.2.1. Particle size and concentration profiles

Integral averaged value and the standard deviation of sand concentration and Rosin–Rammler model parameters for each test point in the measurement plane are shown in Fig. 7 under the condition of $V_m = 1.4$

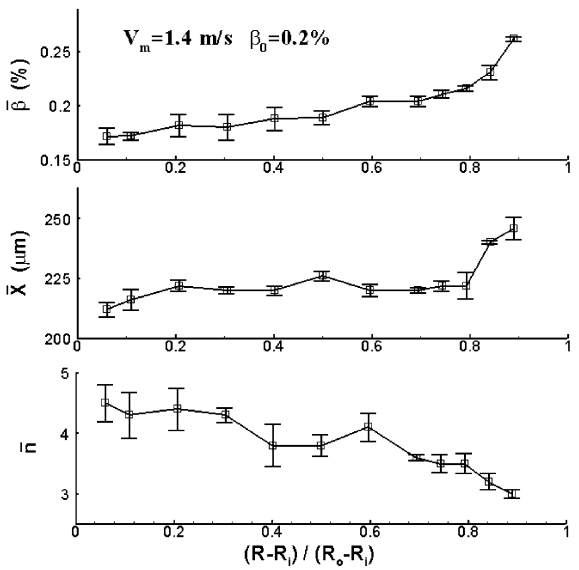

Fig. 7. Sand size and concentration profiles in helically coiled tube two-phase flow.

$m\,s^{-1}$ and $\beta_0 = 0.2\%$. Sand concentration decreases from outer bend to inner bend due to phase separation. Profiles of $\overline{X}$ and $\bar{n}$ reveal some features of phase distribution for a polydisperse system: (1) $\overline{X}$ achieves higher value near outer bend because larger particles are easier to separate; (2) $\bar{n}$ achieves large value near inner bend which corresponds to a narrow particle size range because most of the large particles are driven to outer bend. Fig. 8 presents the concentration profiles for particles larger than 170 μm. It shows that phase separation is more prominent at high water flowrate and sand concentration has little effect on phase separation.

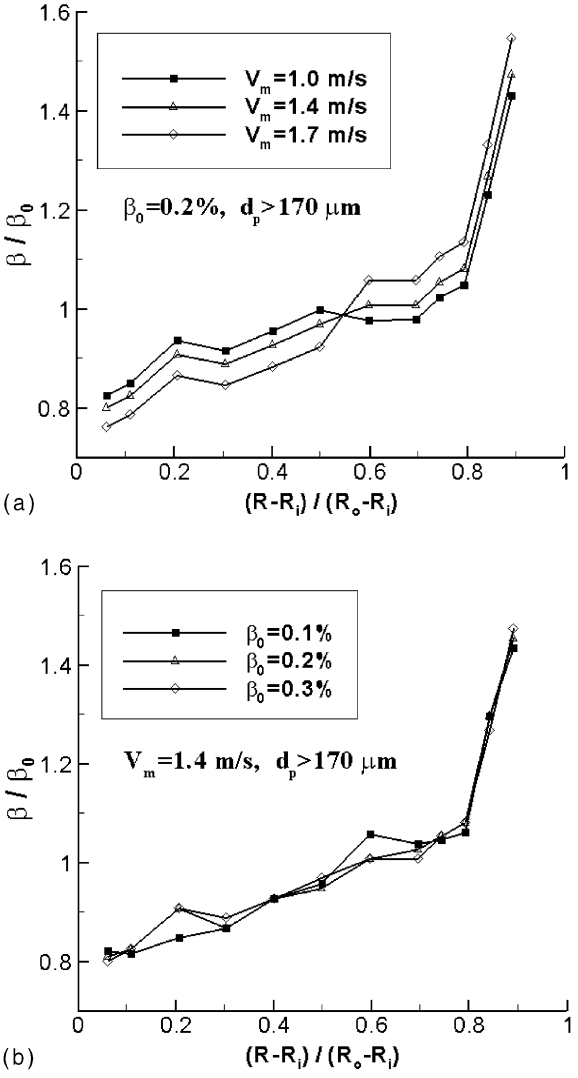

Fig. 8. (a) Effects of V_m on phase separation in helically coiled tube two-phase flow; (b) Effects of β_0 on phase separation in helically coiled tube two-phase flow.

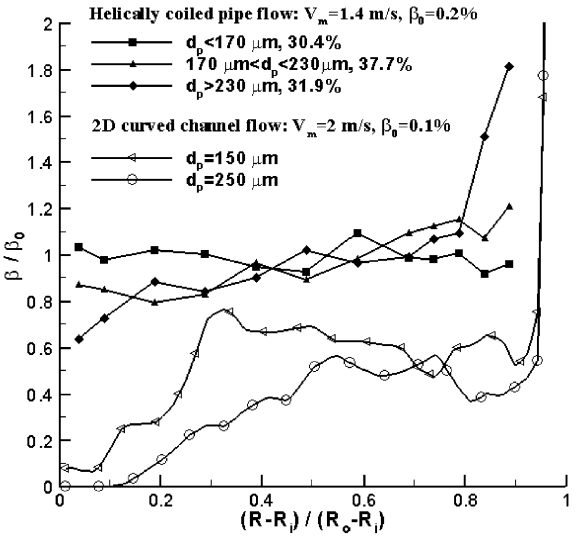

Fig. 9. Comparison of concentration profiles between helically coiled tube flow and 2D curved channel flow.

3.2.2. Comparison between helically coiled tube flow and 2D curved channel flow

Fig. 9 compares the particle concentration profiles in helically coiled tube flow with those in 2D curved channel flow. The polydisperse system in the helically coiled tube flow are divided into three groups which could be approximately considered as monodisperse systems. In general, phase separation is more prominent in 2D curved channel flow. This is due to the dual effects of secondary flow on phase separation: in the central core of cross-section, fluid moves from inner bend to outer bend, which having a positive effect; whereas in the boundary layer region of the side walls, fluid moves from outer bend to inner bend, which having a negative effect. In addition it should be noted that concentration peak also appears for large particles in helically coiled tube flow and that the peak is not so close to outer bend as that of the 2D curved channel flow, indicating that the mouth of particle discharging assembly for the helically coiled tube separator should has a larger height.

4. Analysis and discussion on the affecting factors

The effects of secondary flow and turbulent dispersion on phase separation could be inferred from the above descriptions. Further more, based on the numerical results of the 2D curved channel two-phase flow, dynamic analysis of particle motion was performed to shed light on the effect of centrifugal force and various hydraulic forces. The selection of pipe cross-section was also discussed.

4.1. The effect of centrifugal effect and various hydraulic forces

In the particle dynamic analysis, we focus our interest on: (i) lateral transport procedures of particles released from different positions; (ii) each particle-subjected force's dynamic effect and contribution to separation; and (iii) the kinematic and dynamic difference between large and small particles. Here turbulent dispersion is not included in simulation for convenience.

Two particle samples, i.e. 250 and 100 μm sands were considered. Particles were released at mean liquid velocity from the curved part's entry cross-section. As shown in Figs. 10 and 11, for each particle sample, firstly all particles' transport procedures are illustrated in terms of particle lateral acceleration and lateral displacement, secondly the history of particle-subjected forces for a selected trajectory is depicted and analyzed. In the figures, a particle could be located by two variables, i.e. the curve angle θ and the dimensionless radius ξ which is defined as follows:

$$\xi = (R - R_i)/(R_o - R_i) \tag{7}$$

Fig. 10 illustrates the kinematic and dynamic details of sampled 250 μm sands. The histories of lateral acceleration (with positive direction pointing form inner bend to outer bend) and lateral displacement are plotted for 6 particles released from different positions in Fig. 10(a). Lateral acceleration of each particle increases sharply after the releasing and then undergoes a rapid drop. After that it decreases slowly until the particle approaching outer bend. Finally it undergoes another rapid drop and become negative in outer bend boundary layer. Each particle gains lateral velocity towards outer bend and keeps accelerating in most part of its journey. All sampled particles except the one of $\xi_0 = 0.1$ could

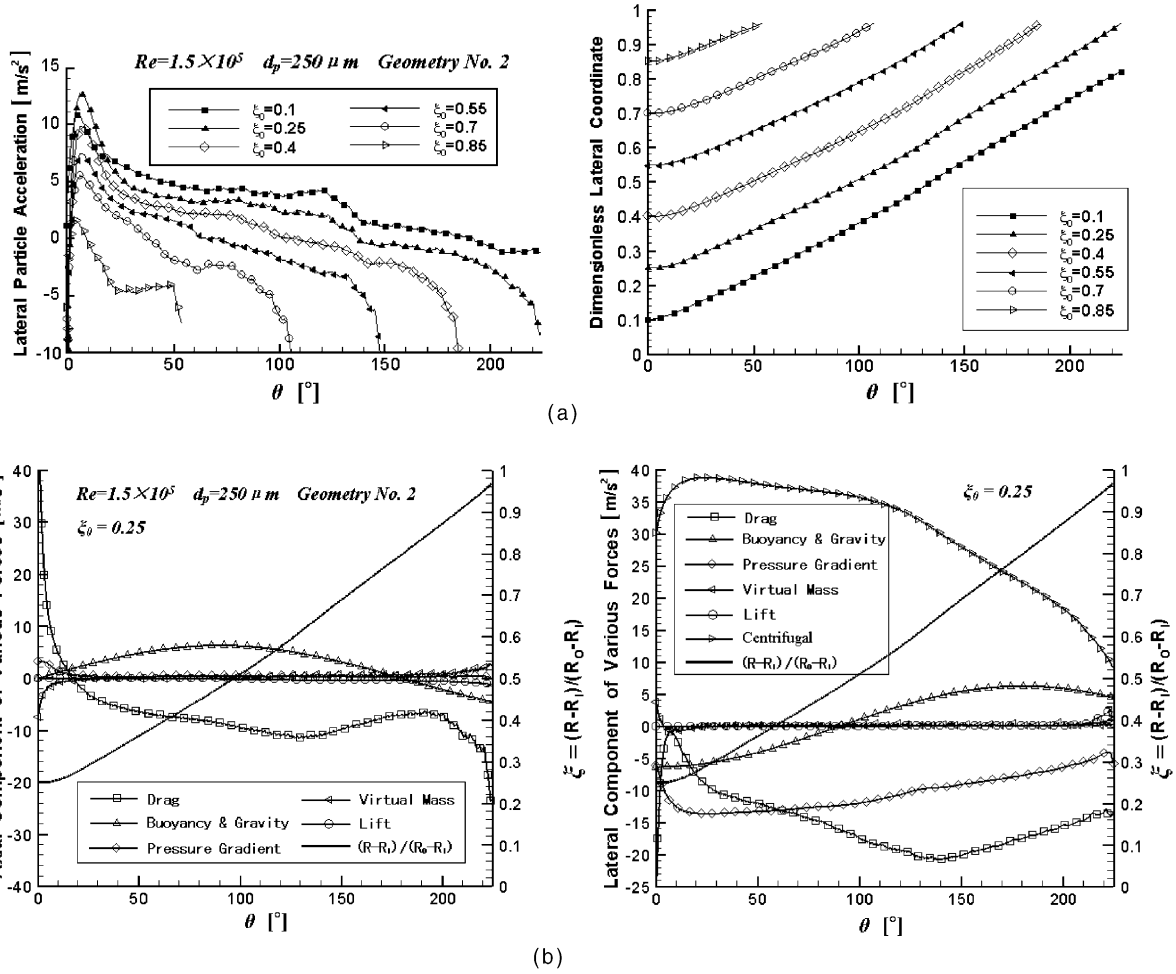

Fig. 10. (a) Lateral transport procedures of 250 μm particles released from different positions; (b) history of particle-subjected forces for a selected trajectory.

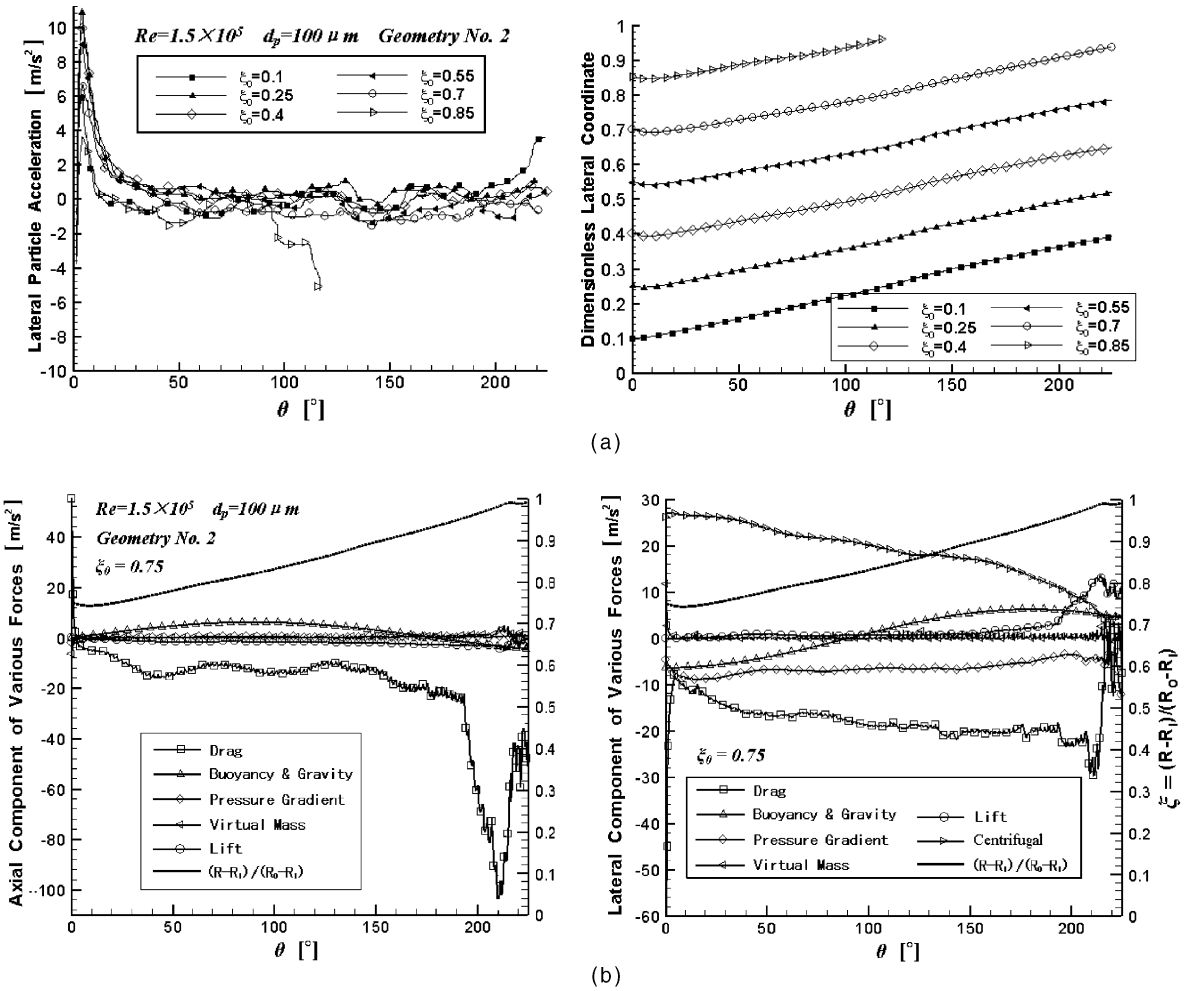

Fig. 11. (a) Lateral transport procedures of 100 μm particles released from different positions; (b) history of particle-subjected forces for a selected trajectory.

reach outer bend. The above described phenomena are ascribed to the colligated effect of all forces acting on each particle.

As shown in Fig. 10(b), each force except the virtual mass one has prominent effect on motion of the selected sand ($\xi = 0.25$). In the streamwise direction, it shows: (i) the drag force component achieves a high positive initial value because its releasing velocity is lower than the local fluid velocity, then it decreases quickly to negative and keeps around $-10\ \mathrm{m\,s^{-2}}$, finally it again undergoes a sharp decrease after entering the boundary layer of outer bend (where $\xi > 0.95$); (ii) the gravity force component keeps varying in magnitude and changes from positive to negative at $\theta = 180°$ because the streamwise direction varies continuously with respect to the vertical one. While in the lateral direction, it shows: (i) centrifugal force plays as the prime driving force for separation, it gradually weakens in the course of particle motion because the particle streamwise velocity continuously decreases; (ii) drag force component plays as the principal retarding effect on particle's lateral displacing, it increases in absolute value in particle lateral accelerating course and then decreases when the particle approaching outer bend; (iii) the pressure gradient force is formed due to the inherent lateral pressure gradient in curved channel flow and resists the particle's lateral motion, with its value decreasing in most course of the particle motion and increasing slightly near outer bend; (iv) the lift force is prominent in outer bend boundary layer where shearing is great, it points to the wall and hence plays as a positive effect on separation; (v) similar to its streamwise counterpart, the lateral component of gravity force varies in magnitude and changes from negative to positive at $\theta = 90°$, hence gravity force has positive effect on sepa-

ration when $\theta = 90$–$270°$ and the present horizontal arrangement of curved channels is reasonable.

Fig. 11 considers the sample of 100 μm sands. Comparing with Fig. 10, it shows that small sands are more difficult to separate. As shown in Fig. 11(a), although each curve of particle lateral acceleration has a peak at its early stage, it fluctuates around or just above the zero value in most course of particle motion; hence particles move slowly in the lateral direction and only the one of $\xi_0 = 0.85$ could reach outer bend. The dynamic characteristics of the small sand, which differs from that of the large one, could be seen from Fig. 11(b) as follows: (i) the lateral component of drag force achieves higher value because the drag coefficient is higher at smaller particle Reynolds number; (ii) lift force are more prominent in outer bend boundary layer.

4.2. Discussion on pipe cross-section design

The above analysis gives us some ideas about how to design the cross-section of curved pipe separator. For the suspension of large particles, since high separation efficiency could be achieved merely by the centrifugal effect, the secondary flow should be restrained. Small cross-section aspect ratio (height over width) is preferred because secondary flow is weak in this situation [13]. As to the suspension including small particles, separation is difficult for 2D curved channel flow even under the conditions of high liquid flowrate and tight channel curvature. Therefore, circular, square or large aspect ratio rectangular cross-section might be a choice; that is, the positive effect of secondary flow should be included to increase separation efficiency, although some measures should be thought up to eliminate or reduce its negative effect.

5. Conclusions

A numerical study of 2D curved channel two-phase flow and experimental investigation of helically coiled tube two-phase flow were conducted to enhance the understanding of liquid–solid separation phenomena and improve the curved pipe separation technique. The particle concentration profiles exist two types which classified as plateau-peak and slope-peak types in 2D curved channel flow. And the concentration peak also appears in helically coiled tube two-phase flow for large particles. It is indicated that the mouth of particle discharging assembly should be designed to just cover the peak. Separation efficiency may be increased by utilizing high liquid flowrate and tight curvature along with increasing number of coils, and hence the pressure loss over the separator would be increased as a sacrifice.

Phase separation is a result of combined effects of centrifugal force, various hydraulic forces, secondary flow and turbulent dispersion. The analysis results show: centrifugal force, which moving particles from inner bend to outer bend, is the prime driving force for separation; drag force and pressure gradient force play an opposite role for separation; lift force is notable near the wall and helpful to separation; virtual mass force could be omitted; turbulent dispersion has negative effect on separation. The secondary flow has dual effects on phase distribution and consequently reduces separation efficiency.

Acknowledgements

This work is supported by the National Science Foundation of China contracted by 59995460-2.

References

[1] G.H. Priestman, J.R. Tippetts, R.R. Dick, Design and operation of oil–gas production separator desanding systems, Chem. Eng. Res. Des., Part A: Trans. Inst. Chem. Eng. 74 (1996) 166–176.
[2] R. Changirwa, M.C. Rockwell, S. Frimpong, J. Szymanski, Hybrid simulation for oil–solids–water separation in oil sands production, Miner. Eng. 12 (12) (1999) 1459–1468.
[3] C.H. Rawlins, S.E. Staten, I.I. Wang, Design and installation of a sand separation and handling system for a Gulf of Mexico oil production facility, in: Proceedings—SPE Annual Technical Conference and Exhibition, Soc. Pet. Eng. (SPE), 2000, pp. 363–372.
[4] L. Guo, Oil–air–water multiphase flow in helically coiled tube and the theory of sand separation from crude oil (in Chinese), J. Eng. Thermalphys. (China) 23 (1) (2002) 107–110.
[5] H. Ito, Flow in curved pipes, JSME Int. J. 30 (262) (1987) 543–551.
[6] X. Chen, L. Guo, Flow patterns and pressure drop in oil–air–water three-phase flow through helically coiled tubes, Int. J. Multiphase Flow 25 (6–7) (1999) 1053–1072.
[7] L. Guo, Z. Feng, X. Chen, Pressure drop oscillation of steam–water two-phase flow in a helically coiled tube, Int. J. Heat Mass Transfer 44 (8) (2001) 1555–1564.
[8] M.R. Kaimal, R. Devanathan, Motion of a viscous fluid with suspended particles in a curved tube, Int. J. Eng. Sci. 18 (1980) 847–854.
[9] Z. Xu, S. Tu, X. Du, Analysis of three-dimensional turbulent flow of mineral slurry in curved pipe (in Chinese), J. Xi'an Jiaotong Univ. 34 (5) (2000) 46–49.
[10] S.A. Morsi, A.J. Alexander, An investigation of particle trajectories in two-phase flow systems, J. Fluid Mech. 55 (2) (1972) 193–208.
[11] R. Mei, An approximate expression for the shear lift on a spherical particle at finite Reynolds number, Int. J. Multiphase Flow 18 (1992) 145–147.
[12] G.M. Faeth, Mixing, transport and combustion in sprays, Prog. Energy Combust. Sci. 13 (1987) 293–346.
[13] M. Akiyama, K. Kikuchi, J. Nakayama, M. Suzuki, I. Nishiwaki, K.C. Cheng, Trans. Japan Soc. Mech. Eng., Part B 47 (421) (1981) 1705.